Materials Today Bio 32 (2025) 101794

Contents lists available at ScienceDirect

Materials Today Bio

journal homepage: www.journals.elsevier.com/materials-today-bio

Curcumin-copper complex nanoparticles as antioxidant nanozymes for acute kidney injury alleviation

Xinyu Huang [a,1], Fengxian Zhang [b,1], Yuan Yang [c,1], Jiawei Liu [b], Xiangyun Tan [a], Peng Zhou [b], Xiaolei Tang [d], Junjie Hu [a], Liang Chen [a], Ming Yuan [a], Guohua Zheng [a,*], Ziqiang Xu [b,**], Zhenpeng Qiu [a,e,f,g,***]

[a] School of Pharmacy, Hubei University of Chinese Medicine, Wuhan, 430065, People's Republic of China
[b] School of Materials Science & Engineering, College of Health Sciences and Engineering, Hubei University, Wuhan, 430062, People's Republic of China
[c] Institute of Maternal and Child Health, Wuhan Children's Hospital (Wuhan Maternal and Child Healthcare Hospital), Tongji Medical College, Huazhong University of Science and Technology, Wuhan, 430016, People's Republic of China
[d] Translational Medicine Center of the Second Affiliated Hospital of Wannan Medical College, Wuhu, 241002, People's Republic of China
[e] Center of Traditional Chinese Medicine Modernization for Liver Diseases, Hubei University of Chinese Medicine, Wuhan, 430065, People's Republic of China
[f] Hubei Key Laboratory of Resources and Chemistry of Chinese Medicine, Hubei University of Chinese Medicine, Wuhan, 430065, People's Republic of China
[g] Hubei Shizhen Laboratory, Wuhan, 430061, People's Republic of China

ARTICLE INFO

Keywords:
Acute kidney injury
Reactive oxygen species
Metal phenolic networks
Copper (II)
Curcumin

ABSTRACT

Acute kidney injury (AKI) is a heterogeneous disorder frequently occurring in hospitalized patients with multiple comorbidities. Chemotherapy-associated AKI (e.g., cisplatin-induced AKI, CP-AKI) and rhabdomyolysis-induced AKI (RM-AKI) are initiated by the excessive accumulation of reactive oxygen species (ROS). Herein, metal phenolic networks (MPNs) composed of copper (II) (Cu^{2+}), a typical cofactor in the native superoxide dismutase (SOD), and a well-studied natural antioxidant curcumin (Cur) (denoted as Cur-Cu) were fabricated to integrate the ROS-scavenging properties of metal ions and polyphenols. The results indicate that Cur-Cu nanoparticles (NPs) possessed robust antioxidative enzyme-like activities. Meanwhile, Cur-Cu NPs with polyethylene glycol (PEG) covalent modification (Cur-Cu@PEG) abolished the ROS-triggered oxidative damage of HK-2 cells. Moreover, Cur-Cu@PEG displayed acceptable biocompatibility *in vivo*. Furthermore, Cur-Cu@PEG alleviated CP-AKI and RM-AKI in mice with kidney-targeted delivery. Mechanistically, Cur-Cu@PEG effectively lessened the production of ROS, thereby repressing caspase-3-dependent apoptotic/pyroptotic cell death in the kidneys of AKI mice. Altogether, these results offer a viable approach for synthesizing antioxidant metal phenolic networks mimics to ameliorate ROS-related diseases.

1. Introduction

Acute kidney injury (AKI) is manifested as an acute severe decline in renal excretory function [1] induced by multi-factors, such as chemotherapies, rhabdomyolysis, ischemia, urinary tract obstruction, and sepsis [2,3], which commonly contributes to about 1.7 million deaths globally annually [4]. Cytotoxic chemotherapeutic agents, such as cisplatin (CP), repress the malignant transformation of cancer cells by enhancing reactive oxygen species (ROS) generation [5]. Meanwhile, chemotherapies-induced ROS accumulation disrupts the balance of oxidative stress and antioxidant defense system, resulting in the damage and destruction of bio-molecules of renal cells [6]. Furthermore, mounting evidence suggests that pyroptosis is essential in cisplatin-induced AKI (CP-AKI) [7]. Once activated by ROS, caspase-3 further triggers the cleavage of Gasdermin E (GSDME), which functions as a N-terminal fragment puncturing the cell membrane and subsequently initiates pyroptosis [8,9]. Also, AKI is a life-threatening complication of rhabdomyolysis. Rhabdomyolysis-induced AKI

---

* Corresponding author.
** Corresponding author.
*** Corresponding author. School of Pharmacy, Hubei University of Chinese Medicine, Wuhan, 430065, People's Republic of China.
E-mail addresses: zgh1227@sina.com (G. Zheng), ziqiang.xu@hubu.edu.cn (Z. Xu), qiuz@hbucm.edu.cn (Z. Qiu).
[1] Xinyu Huang, Fengxian Zhang, and Yuan Yang contributed equally to this work.

https://doi.org/10.1016/j.mtbio.2025.101794
Received 12 November 2024; Received in revised form 16 April 2025; Accepted 22 April 2025
Available online 23 April 2025

(RM-AKI) accounts for 10 % of all instances of AKI [10]. The release of myoglobin from injured muscles leads to AKI by creating blockage in the tubules, constricting blood vessels in the kidneys, and further triggering oxidative stress in proximal tubules [11]. Hence, the reduction in excessive ROS production could substantially benefit the management of AKI. Although N-acetyl cysteine (NAC) is a clinical antioxidant drug for AKI therapy, the high-dose usage and low bioavailability of NAC restrain its efficient utilization [12].

Recently, nanomaterial-based cellular antioxidant enzyme mimics showing efficacy in mitigating oxidative stress have emerged as a potential approach for overcoming the limitations in AKI alleviation due to the higher stability and versatile enzyme simulation selectivity of these nanozymes [13,14]. Moreover, various nanozymes, including noble metal nanoparticles, metal oxides nanoparticles, prussian blue nanoparticles, and carbon nanomaterials [15], have been discovered for ROS scavenging and therapies of inflammatory diseases. Owing to the superior ROS scavenging properties and biocompatibilities, natural phenolic compounds have been widely used for fabricating antioxidative nanozymes, especially metal phenolic networks (MPNs) [16,17]. MPNs are a class of metal-organic framework-based nanomaterials composed of catechol or gallol groups coordinating with various metal ions, which are considered the fascinating nanozymes in the therapy of AKI due to their adjustable functionality *via* varying natural polyphenols and metal ions [17,18]. Furthermore, MPNs-based antioxidant nanozymes simultaneously integrate the advantages of inherent antioxidant capacities, high biocompatibility of natural phenols, and distinct properties of metal ions, including electronic, magnetic, and optical properties [19]. Notably, the metal-phenolic combination would generate core-satellite nanostructure assemblies [20,21], affording enormous flexibility to manipulate and augment the redox properties of noble metal nanoparticles.

Furthermore, the pharmacokinetic properties of natural phenols in MPNs with ultra-small diameters and eminent stabilities were also optimized [22]. MPNs-based nanozymes with superior antioxidant properties have been utilized to remedy oxidative stress-implicated diseases [17,23]. Copper (II) (Cu^{2+}), indispensable for the catalytic activity of native superoxide dismutase (SOD) in mammalian cells, is typical and valuable metal ions for the fabrication of MPNs. In this study, natural antioxidants, including curcumin (Cur), tannic acid (TA), caffeic acid (CA), resveratrol (RE), and epigallocatechin (EGCG), are coordinated with low-toxic Cu^{2+} to form ultra-small MPNs, including Cur-Cu, TA-Cu, CA-Cu, RE-Cu, and EGCG-Cu (Fig. S1), which displayed considerable dispersibility and stability. Among these, Cur-Cu nanoparticles (NPs) with ultra-small size and superior dispersity, which is conducive to improving bioavailability and stability. In addition, Cur itself has good antioxidant and anti-inflammatory capabilities, and has strong metal chelating ability to stabilize Cu^{2+}, reduce the oxidative damage caused by the Fenton reaction, and Cu^{2+} has antioxidant activity and promotes angiogenesis and tissue repair. Therefore, the Cur-Cu NPs perfectly combines the properties of Cur and Cu^{2+}, which is conducive to showing excellent effects in antioxidant and anti-inflammatory treatments. This study further evaluated the antioxidant activity of Cur-Cu NPs, and the results showed that it has excellent broad-spectrum antioxidant capacity and can effectively scavenge a variety of ROS. Cur-Cu@PEG attenuates ROS-induced human renal tubular epithelial HK-2 cell death and oxidative stress *in vitro* and alleviates AKI in mice by suppressing caspase-3-dependent apoptotic/pyroptotic cell death (Scheme 1). Overall, these results provide valuable insights into the application of natural product-loaded nanomedicines as promising therapeutic approaches for ROS-related disorders.

2. Materials and methods

2.1. Measurements

The average size and Zeta potential were obtained with a Malvern Zetasizer ZS90 nano-granularity analyzer. The ultraviolet–visible (UV–Vis) spectroscopy were recorded using a UV–visible spectrophotometer (Meipuda UV-1800 PC). Fluorescent (FL) spectra were recorded by the Shimadzu fluorescence spectrometer (RF-6000). Fourier transform infrared (FT-IR) spectra were obtained by the Shimadzu IR Prestige-21 spectrometer. X-ray photoelectron spectra (XPS) were obtained by the Thermo Escalab 250Xi. Electron spin resonance (ESR) spectra were recorded by Bruker A300 at room temperature. The fluorescent images were taken by both the Leica DMi8 CLSM and the Olympus fluorescence microscope. The cell behavior was analyzed by

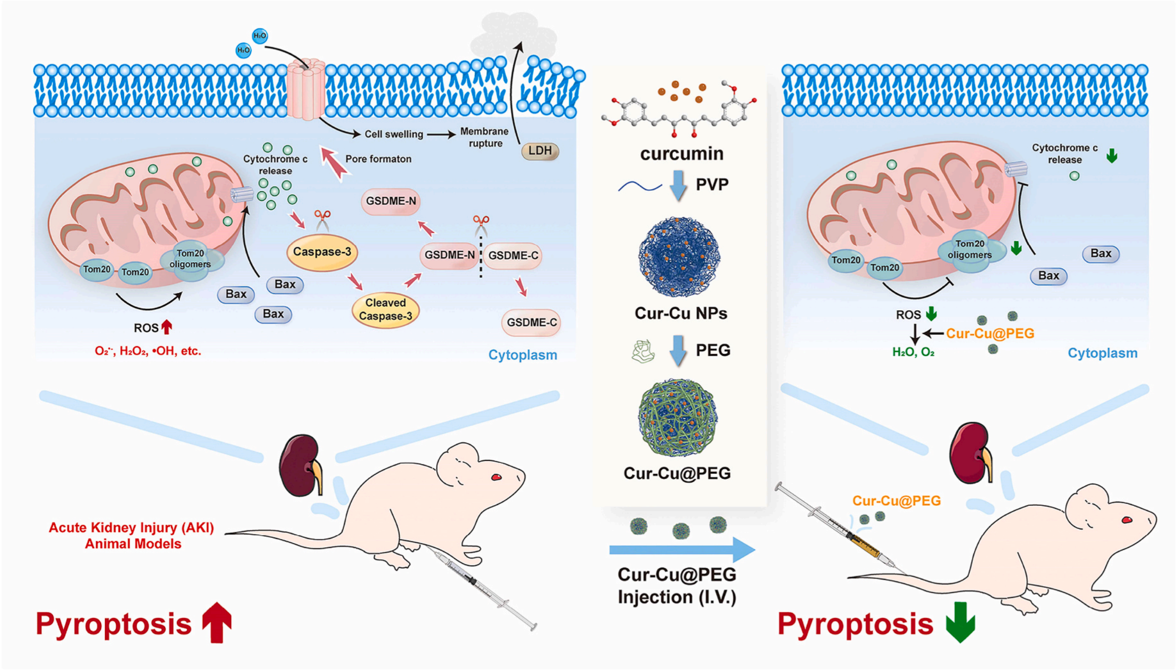

Scheme 1. Schematic illustration of the fabrication of Cur-Cu@PEG with multifunctional antioxidant activities. Cur-Cu@PEG shows efficacy in mouse models of acute kidney injury (AKI) by suppressing caspase-3-dependent programmed cell death *via* ROS elimination.

ACEA Novo Cyte D2060R flow cytometry.

2.2. Synthesis of Cur-Cu NPs

Firstly, 30 mg copper chloride ($CuCl_2$) •$2H_2O$ was dissolved in 10 mL of deionized water, and 60 mg Cur dissolved into 10 mL dimethyl sulfoxide (DMSO) was drop-wisely added accompanied by stirring for 15 min. 200 mg polyvinylpyrrolidone (PVP) dissolved into 10 mL deionized water was drop-wisely added, followed by 8 h of stirring at 60 °C. The solution was dialyzed against deionized water for 7 days. The obtained Cur-Cu NPs were freeze-dried for further use.

2.3. Surface modification of Cur-Cu NPs

The pH of Cur-Cu NPs aqueous solution (10 mL; 5 mg/mL) was adjusted to 8.5 with NH_4OH aqueous solution (28 wt%), followed by dropwise addition to 1,2-distearoyl-sn-glycero-3-phosphoethanolamine-N-[methoxy(polyethylene glycol)-2000] (DSPE-PEG2k) aqueous solution (15 mL; 10 mg/mL of DSPE-PEG2k) under 12 h of stirring. PEG-modified Cur-Cu NPs were collected by ultrafiltration (M_WCO: 30 kDa) and washed with deionized water. The obtained Cur-Cu@PEG aqueous solution was freeze-dried for further use.

2.4. 2,2′-azino-bis (3-ethylbenzothiazoline-6-sulfonic acid) (ABTS) radical scavenging assay

The ABTS (7.4 mM) and $K_2S_2O_8$ (2.6 mM) solutions were mixed and stored in the dark at room temperature for 12 h. The aqueous solutions of Cur-Cu NPs at different concentrations (12.5, 25, 50, 100, and 200 μg/mL) were added to 50 times PBS-diluted ABTS solution and incubated in the dark for 10 min. The ratio of neutralized ABTS$\bullet^+$ to total ABTS$\bullet^+$, reflecting ABTS$\bullet^+$ scavenging activity was assessed using a UV–visible spectrophotometer at 734 nm.

2.5. 2,2-Diphenyl-1-picrylhydrazyl (DPPH) radical scavenging assay

Different concentrations of Cur-Cu NPs (12.5, 25, 50, 100, and 200 μg/mL) were incubated in 1 mL of ethanolic DPPH (60 μM) solution or in ethanol (as a control). The reactions were incubated for 30 min at room temperature, and the absorbance of reactions was measured at 515 nm using a UV–visible spectrophotometer. The DPPH• scavenging activity was calculated as the ratio of neutralized DPPH• to total DPPH•.

2.6. Superoxide anion ($O_2^{\bullet-}$) and hydroxyl radical (•OH) scavenging assays

The $O_2^{\bullet-}$ and •OH scavenging activities of Cur-Cu NPs at different concentrations (12.5, 25, 50, 100, and 200 μg/mL) were analyzed using commercial SOD and •OH assay kits. The reaction system and conditions were configured according to the manufacturers' instructions. The inhibition rates for $O_2^{\bullet-}$ and •OH scavenging were calculated using equations $D\% = [(A_B\text{-}A_{BC})\text{-}(A_T\text{-}A_{TC})]/(A_B\text{-}A_{BC})*100\ \%$ and $D\% = (A_T\text{-}A_C)/(A_B\text{-}A_C)*100\ \%$, respectively.

2.7. Hydrogen peroxide (H_2O_2) scavenging assay

Briefly, H_2O_2 (500 mM) was added to a 50 mL flask plugged with a butyl rubber plug. The oxygen concentrations were recorded using a portable dissolved oxygen meter (JPB-607A) with an oxygen electrode probe. Once the oxygen concentration reached equilibrium in the closed system, Cur-Cu NPs at different concentrations (25, 50, 100, 200, and 400 μg/mL) were added, and the oxygen concentrations were further determined.

2.8. Lactate dehydrogenase (LDH) release assay

LDH is a stable cytoplasmic enzyme. The level of LDH release reflects the degree of pyroptosis [8]. Levels of LDH released into the supernatants of HK-2 cells exposed to oxidative stress, either in the absence or presence of various concentrations (0–6.4 μg/mL) were quantified using the LDH Cytotoxicity Assay Kit II from Beyotime (Shanghai, China).

2.9. Biodistribution

Cur-Cu NPs and rhodamine B-poly(ethylene glycol)-thiol (RB-PEG-SH) were dissolved in deionized water separately. The Cur-Cu NPs solution was stirred for 1 h using a magnetic stirrer at 500 rpm. Then, twice the volume of RB-PEG-SH solution was slowly added to the Cur-Cu NPs solution, and the mixture was stirred for an additional 8 h. The solution was further dialyzed against deionized water overnight using a dialysis bag (M_W: 3500 Da) to produce Rhodamine B (RB)-labeled Cur-Cu@PEG, which was then freeze-dried for biodistribution evaluation. RB-labeled Cur-Cu@PEG (0.5 mg dissolved in 100 μL PBS) was intravenously injected into Institute of Cancer Research (ICR) mice. The injected mice were sacrificed, and the main visceral organs were collected at predetermined intervals. Images were captured using an IVIS Lumina imaging system (Xenogen Corporation, Alameda, USA). Living Image 4.2 was utilized to measure organ fluorescence signals. Rhodamine B: $\lambda_{em} = 525$ nm, $\lambda_{ex} = 488$ nm.

2.10. AKI model establishment and administration

The animal experiment procedures were authorized by the Institutional Animal Care Usage Committee of the Hubei University of Chinese Medicine (No. HBCMS202211001). To establish a RM-AKI model, ICR mice with free access to food were subjected to 16 h of water deprivation. The water-restricted mice subsequently received an intramuscular injection of 8 mL/kg of 50 % glycerol in the hind limbs. The CP-AKI mouse model was established by intraperitoneal injection of CP (20 mg/kg). Cur-Cu@PEG (0.5 mg dissolved in 100 μL PBS) was intravenously administered 2 h post injection of glycerol and CP. RM-AKI and CP-AKI mice were euthanized 24 h post glycerol injection and 72 h post CP injection, respectively. Blood and renal samples from the mice were collected for further evaluation.

2.11. Terminal deoxynucleotidyl transferase dUTP nick end labelling (TUNEL) and dihydroethidium (DHE) staining

TUNEL staining procedure was conducted using an *In Situ* Cell Death Detection Kit from Roche (Basel, Switzerland). For DHE staining, frozen kidney tissue slices (approximately 5 μm thickness) were rinsed with PBS and incubated in the dark with 1 mM DHE for 30 min. The slices were washed three times with PBS and incubated with 4′,6-diamidino-2-phenylindole (DAPI) for 10 min. DAPI/DHE-stained samples were washed and then sealed with an anti-fluorescent quenching agent. Cellular fluorescence was captured using a fluorescence microscope.

2.12. Immunohistochemistry (IHC) and immunoblotting

For the IHC assay, mouse kidney tissue slices embedded in fixed paraffin were subjected to dehydration employing a series of ethanol treatments with varying concentrations. The processed sections underwent antigen retrieval in citrate buffer (pH 6.0). The microscope slides were blocked with 2.5 % normal goat serum and incubated with a primary antibody overnight at 4 °C. The PBS-washed slides were stained with a SP Rabbit & Mouse HRP Kit according to the manufacturer's instructions. The immunohistochemical stains were photographed using a microscopy.

HK-2 cells and renal tissue samples were lysed with the M-PER buffer containing protease and phosphatase inhibitors for immunoblotting.

Protein concentrations were quantified using the BCA protein assay. Heat-denatured protein samples (20–40 μg) in sodium dodecyl sulfate (SDS) solution were separated by SDS-PAGE electrophoresis. Separated proteins were transferred to polyvinylidene fluoride (PVDF) membranes and blocked with 5 % skim milk for 2 h. The membranes were incubated with primary antibodies overnight, washed with TBS containing 0.1 % Tween 20 for 10 min, and then incubated with a horseradish peroxidase (HRP)-conjugated secondary antibody for 1 h. The immunoblots were visualized using a chemiluminescent method. Densitometric analysis was performed with ImageJ software (version 1.51).

2.13. Statistical analysis

Quantitative data were presented as mean ± standard deviation (S.D.). All data were expressed as Mean ± S.D. values. ANOVA was performed among three or more groups, respectively. Differences were accepted as statistically significant at a *P*-value lower than 0.05.

3. Results and discussion

3.1. Synthesis and characterization of Cur-Cu NPs

Due to the Cu^{2+} chelation capacity of natural phenolic compounds, MPNs with adjustable structures can be assembled from different phenolic building blocks. The MPNs-based nanoparticles were fabricated by mixing Cu^{2+} with multiple the natural products (Cur, TA, CA, RE, and EGCG) dissolved in a DMSO solution, respectively. During the formation process, PVP was introduced to control the growth of nanometric MPNs with the stability of aqueous dispersion *via* the hydrophobic repulsive force of PVP. A color change of the synthetic system from blue to yellow, which ultimately turns to pitch-dark, suggests that the phenolic hydroxyl groups in natural products were efficiently coordinated with Cu^{2+}. Finally, the solutions were dialyzed against deionized water for 7 days to remove uncombined Cu^{2+}, phenolics and PVP.

The morphology and size of each MPNs were characterized by a transmission electron microscope (TEM). The morphology of MPNs was quasi-sphere and separated from each other. The result indicated that CA-Cu NPs with small diameters (approximately 4.8 nm) were aggregated into large-sized clusters (40–60 nm) (Fig. S1A). EGCG-Cu, TA-Cu, and RE-Cu NPs displayed a similar effect of agglomerates, from 12 nm to 80–100 nm, 5.81 nm–150 nm, and 5.49 nm–100 nm in TEM analysis, respectively (Fig. S1B–D). Notably, the diameter of smaller Cur-Cu NPs was estimated to be about 5.8 nm, which guarantees a potential kidney-specific enrichment of Cur-Cu NPs *in vivo* (Fig. 1A) [24,25]. Moreover, dynamic light scattering (DLS) indicated that the hydrodynamic size of Cur-Cu NPs was below 10 nm, while that of other MPNs could be up to hundreds of nanometers (Fig. S2A), which is attributed to the inherent aggregation properties of these MPNs in aqueous environments. The Zeta potential of MPNs is negatively charged and close to neutral, which is beneficial for prolonged blood retention *in vivo* (Fig. S2B). Therefore, Cur-Cu NPs were selected for the following experiments.

The detailed coordination process of Cur-Cu NPs is further presented in. Briefly, Cur dissolved in DMSO was added drop-wisely to a round-bottom flask containing the pH-adjusted $CuCl_2$ solution at pH 12. The PVP solution was further drop-wisely added and stirred at 60 °C for 8 h to obtain Cur-Cu NPs. As shown in the TEM images (Fig. 1A), Cur-Cu NPs presented average sizes of around 5.8 nm, which almost agrees with the results obtained from the DLS analysis, indicating its good water dispersibility (Fig. S2A). Fig. S2C shows that the particle size of Cur-Cu NPs remains nearly consistent in different solutions, indicating their excellent stability. The UV–Vis spectra of Cur-Cu NPs (Fig. 1B) shows a typical absorption peak of Cur at 420 nm, confirming the presence of Cur in the Cur-Cu NPs. Cur-Cu NPs also exhibit significant fluorescence peaks within the range of 340–460 nm under different excitation wavelengths, indicating the formation of coordination polymers composed of Cu^{2+} and Cur (Fig. S3A). FT-IR and XPS were performed to analyze the structural details of Cur-Cu NPs. The FT-IR spectra analysis indicated the existence of abundant oxygen-containing functional groups on the surface of Cur-Cu NPs (Fig. 1C). The absorption peak for -OH stretching occurring at 3444 cm^{-1} was related to the hydroxyl of curcumin and absorbed water. The most intense peak at 1658 cm^{-1} was related to the

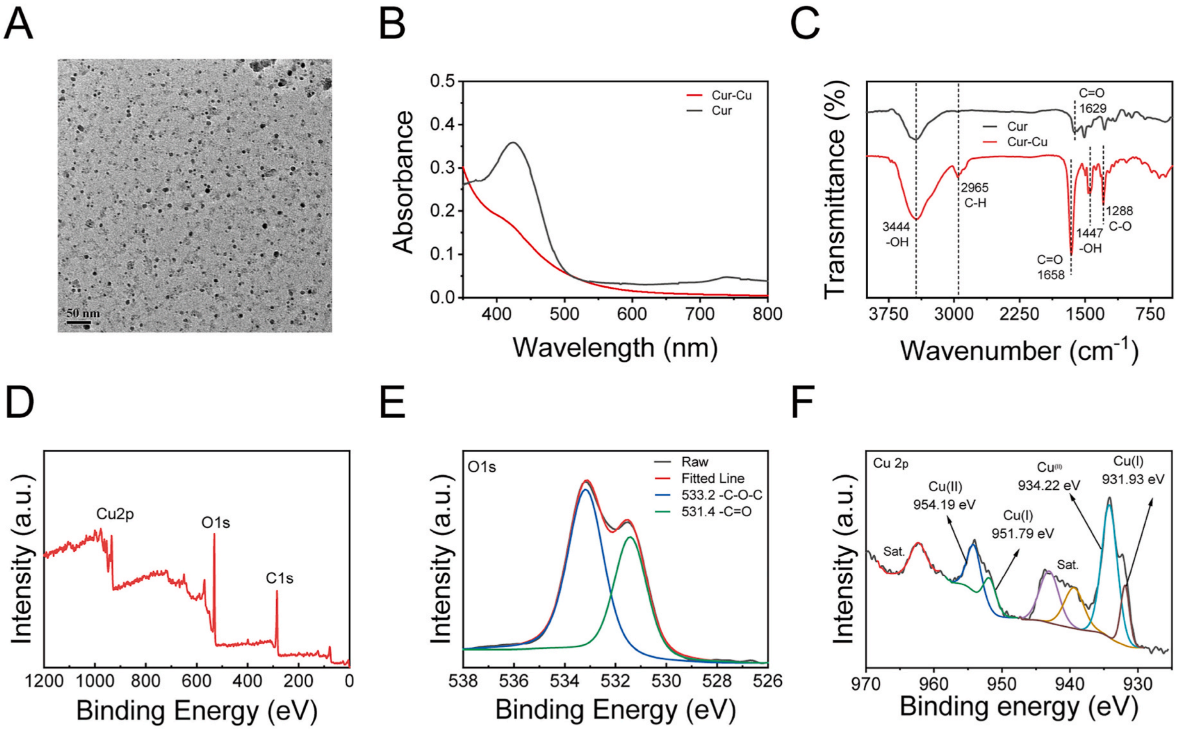

Fig. 1. Characterization of Cur-Cu NPs. **(A)** TEM image of Cur-Cu NPs. **(B)** Absorption spectra of Cur-Cu NPs and curcumin (Cur). **(C)** FT-IR spectra of Cur-Cu NPs and Cur. **(D)** XPS survey spectrum of Cur-Cu NPs. **(E–F)** High resolution spectrum of O1s (E) and Cu2p (F) of Cur-Cu NPs.

stretching vibration of C=O and confirmed the presence of PVP in Cur-Cu NPs. The vibration at 2965 cm^{-1} was attributed to C-H stretching from the alkane chain of PVP, and the peak at 1288 cm^{-1} was caused by the vibrations of C-N from PVP. In agreement with the UV–Vis analysis, the shift and appearance of the two peaks at 1660 and 1642 cm^{-1} indicated the coordination of Cu^{2+} and C=O moieties of curcumin [26], suggesting that there were abundant functional groups on the surface of Cur-Cu NPs. XPS was performed to assess the surface chemical valence and chemical composition of Cu atoms in Cur-Cu NPs. The XPS results of Cur-Cu NPs indicated the presence of C1s, O1s, and Cu2p, which corresponded to peaks at 284.0, 531.9, and 934.78 eV, respectively (Fig. 1D). The high-resolution XPS of C1s spectrum suggested that Cur-Cu NPs consisted of two peaks corresponding to C-C and C=O at 284.4 and 287.5 eV, respectively (Fig. S3B). The high-resolution O1s spectrum for Cur-Cu NPs was fitted with two components assigned to C=O and C-O-C at 531.4 eV and 533.2 eV, respectively (Fig. 1E). The Cu2p spectrum exhibited two peaks at 931.93 and 951.79 eV, which could be ascribed to Cu(I) (Fig. 1F). Additionally, two peaks at 932.22 and 954.19 eV, together with satellite peaks around 939.32, 943.06, and 962.36 eV, could all be assigned to Cu(II) 2p peaks (Fig. 1F), potentially indicating the co-presence of Cu(I) and Cu(II) in Cur-Cu NPs [27,28].

3.2. ROS scavenging activities of Cur-Cu NPs

Emerging evidence suggests that •OH, O$_2^{\bullet-}$, and H$_2$O$_2$ are representative ROS hindering redox homeostasis during AKI progression [29]. The superabundant formation of •OH contributes to oxidative damage of cellular DNA and membranes [30]. The •OH elimination efficiency of Cur-Cu NPs was assessed using 3,3′,5,5′-tetramethylbenzidine (TMB) as a probe that can be converted to blue ox-TMB by •OH with prominent absorption peaks at 652 nm. The •OH is produced through the classic Fe^{2+}/H$_2$O$_2$ Fenton reaction in an aqueous solution [30]. As shown in Fig. 2A, a significant absorption peak at 652 nm in the reaction system gradually decreases in the presence of different concentrations of Cur-Cu NPs, suggesting that Cur-Cu was capable of scavenging •OH. The •OH scavenging assay further indicated that the inhibition rate of •OH reached 80 % at 200 μg/mL of Cur-Cu NPs (Fig. 2B). ESR experiments were conducted to determine the •OH radical-eliminating capacity of Cur-Cu NPs [31]. The disappearance of the •OH characteristic peak in ESR assays demonstrates that Cur-Cu NPs can effectively eliminate •OH (Fig. 2C). In addition, TMB is regarded as a chromogenic substrate for peroxidase (POD), and it was selected as an electron donor to evaluate the POD-like activity of Cur-Cu NPs. Once HRP was added, the ox-TMB production showed maximum absorbance at 652 nm. In contrast, a significant absorption peak at 652 nm did not occur when Cur-Cu NPs

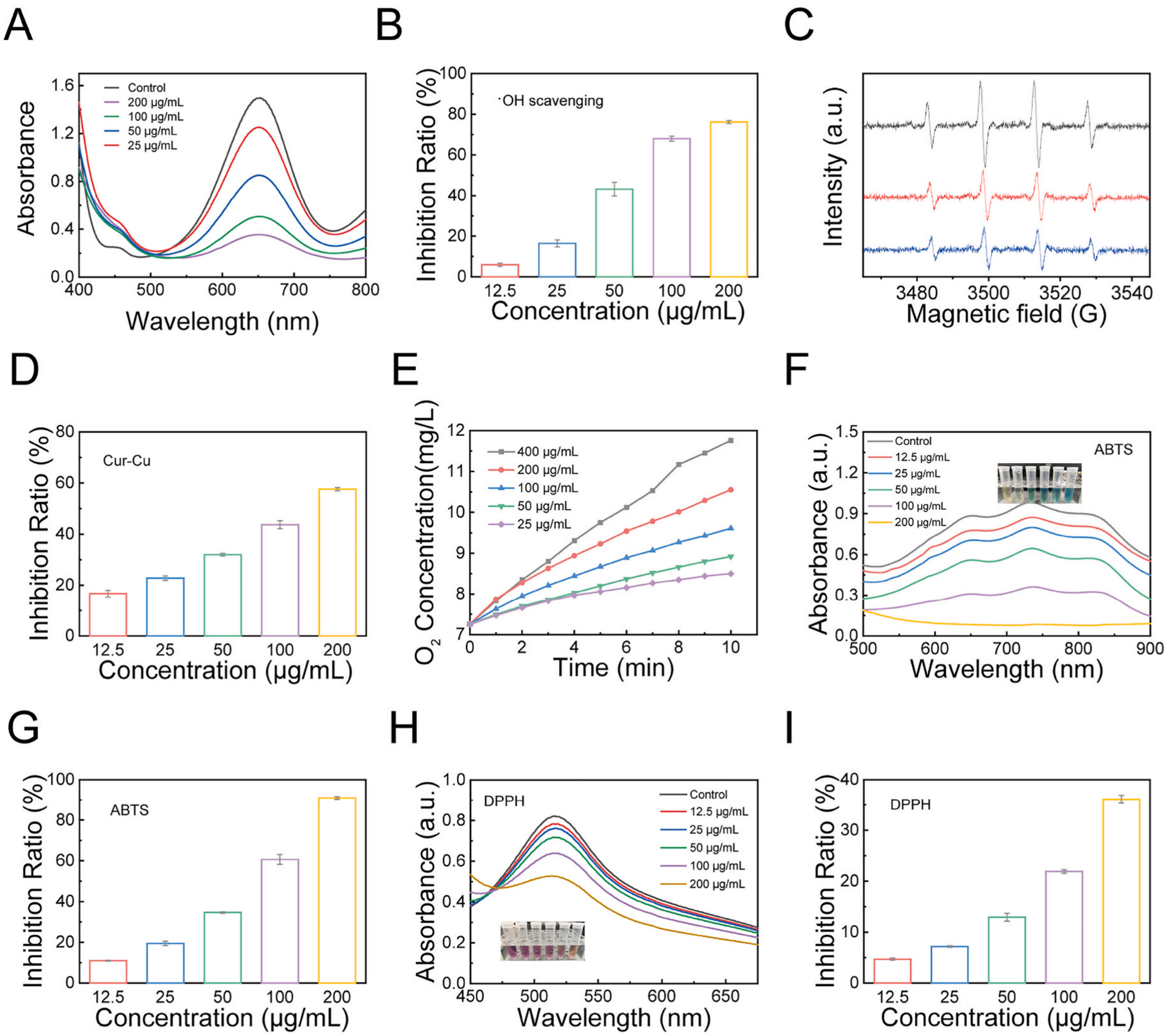

Fig. 2. ROS scavenging activities of Cur-Cu NPs. **(A)** Absorption spectrum of ox-TMB in the presence of Cur-Cu NPs. **(B)** ·OH scavenging activity of Cur-Cu NPs. **(C)** ESR spectra of Cur-Cu NPs reacted with ·OH. **(D)** SOD-like activity of Cur-Cu NPs. **(E)** O$_2$ generation from H$_2$O$_2$ catalyzed by Cur-Cu NPs. **(F)** UV–vis spectra of free radicals ABTS•$^+$ in the presence of Cur-Cu NPs. **(G)** ABTS scavenging activity of Cur-Cu NPs. **(H)** Absorbance spectrum of DPPH• in the presence of Cur-Cu NPs. **(I)** DPPH scavenging activity of Cur-Cu NPs.

were introduced, indicating that POD activity is absent in Cur-Cu NPs. POD-like activity has been observed in various transition-metal-based nanoparticles, including metal oxides or metal coordination-based nanomaterials [32,33], which could effectively catalyze the conversion of H_2O_2 into •OH. Furthermore, Cur-Cu NPs displayed negligible POD-like activity in different pH buffer solutions (pH = 4.0, 6.5, and 7.4), further indicating that Cur-Cu NPs barely produced few •OH to exert side effects (Fig. S4A). Furthermore, a commercial WST-1-based SOD assay kit was used to examine the $O_2^{\bullet -}$ scavenging ability of Cur-Cu NPs. WST-1 reacts with the generated $O_2^{\bullet -}$ from the xanthine and xanthine oxidase, causing an apparent increase in characteristic absorption at 450 nm [34]. The absorptions were significantly reduced in the presence of Cur-Cu NPs, indicating that Cur-Cu NPs possess excellent $O_2^{\bullet -}$ removing properties. Meanwhile, the elimination rate of $O_2^{\bullet -}$ was elevated to 57 % upon 200 μg/mL of Cur-Cu NPs incubation, demonstrating the superior SOD-like activity of Cur-Cu NPs (Fig. 2D). The antioxidant enzyme catalase (CAT) governs the conversion of H_2O_2 into H_2O and O_2 [35]. Here, the CAT-mimicking activity of Cur-Cu NPs was further evaluated using a dissolved oxygen (DO) meter. A dose-dependent increase in O_2 production was observed in the presence of Cur-Cu NPs with different concentrations (25, 50, 100, 200, and 400 μg/mL), indicating that Cur-Cu NPs showed a solid dose-dependent CAT-like activity (Fig. 2E). The total antioxidant capacity (TAC) of Cur-Cu NPs was investigated using $ABTS\bullet^+$ and DPPH• as typical indicators [36]. The evident decrease in the absorbance of $ABTS\bullet^+$ at 734 nm was elicited by Cur-Cu NPs at various concentrations (12.5–200 μg/mL) (Fig. 2F–G). Strikingly, approximately 91 % of $ABTS\bullet^+$ was eliminated by Cur-Cu NPs at a concentration of 200 μg/mL (Fig. 2F–G). Cur-Cu NPs also caused apparent losses of initial absorption of the stable nitrogen radical DPPH• at 515 nm in a dose-dependent manner, indicating that Cur-Cu NPs could donate the H atom for their superior antioxidant capacities (Fig. 2H–I). Together, these results demonstrate that Cur-Cu NPs possess superior ROS-scavenging activities.

3.3. *Cytoprotective effects of Cur-Cu@PEG*

Owing to multienzyme-like activities, the antioxidant properties of Cur-Cu NPs were further investigated in ROS-accumulated cellular context *in vitro*. However, unmodified Cur-Cu NPs elicited apparent cytotoxicity in HK-2 cells (Fig. S5). To improve the biocompatibility of Cur-Cu NPs, DSPE-PEG2k was introduced onto the surface of Cur-Cu NPs *via* the hydrophobic interactions between 1,2-distearoyl-sn-glycero-3-phospho-ethanolamine (DSPE) and PVP at pH = 8.5 to obtain Cur-Cu@PEG. As shown in Fig. S6A, Cur-Cu@PEG exhibits uniformly dispersed carbon nanospheres with a diameter of about 7.6 nm, indicating that PEG modification does not significantly change the morphology and size of Cur-Cu NPs. In addition, Fig. S6B further shows that the hydrated particle size of Cur-Cu@PEG after PEG modification increases slightly, while there is no significant change. The Zeta potential in Fig. S6C shows that the surface charge of Cur-Cu@PEG is similar to that of Cur-Cu NPs, both being close to neutral. This helps prolong its retention time in the body, thereby enhancing the therapeutic effect. We further evaluated the stability of Cur-Cu@PEG which may affect their efficacy and safety. As shown in Fig. S6D, the particle size variation of Cur-Cu@PEG in various solutions is not obvious, indicating that they have excellent stability and can be further tested *in vitro* and *in vivo*. The cell survival rates of HK-2 cells treated with Cur-Cu@PEG remained above 80 % at the concentration of up to 100 μg/mL, showing considerably lower cytotoxicity of Cur-Cu@PEG compared to Cur-Cu NPs (Fig. 3A). The cytoprotective and antioxidant capacities of Cur-Cu@PEG were further estimated in HK-2 cells exposed to CP and H_2O_2. CP readily reacts with glutathione and other antioxidant substances that contain sulfhydryl groups, leading to cellular oxidative stress [37]. Cur-Cu@PEG pre-treatment at concentrations ranging from 0.1 to 6.4 μg/mL increased cell viability by up to approximately 30 % (Fig. 3B–C). Further, 2′,7′-dichlorofluorescein diacetate (DCFH-DA) was employed to determine ROS levels of HK-2 cells [38]. Cur-Cu@PEG treatment reduced the green fluorescent signals (Fig. 3D–E and Fig. S7-8). The influence of Cur-Cu@PEG on HK-2 cell death triggered by CP/H_2O_2 was measured using Annexin V-fluorescein isothiocyanate (FITC)/propidium iodide (PI) or calcein acetoxymethyl ester (calcein-AM)/PI double labeling kits. The results indicated that Cur-Cu@PEG treatment antagonized ROS-induced programmed cell death (PCD) *in vitro* (Fig. 3F–G and Fig. S9-10).

3.4. *Biocompatibility and biodistribution of Cur-Cu@PEG in vivo*

The *in vivo* toxicity and safety analysis of Cur-Cu@PEG were further investigated. Compared to the control animals receiving the same volume of vehicle (PBS), ICR mice intravenously injected with Cur-Cu@PEG showed no abnormal histological alterations in internal organs (heart, liver, spleen, lungs, and kidneys) with no abnormalities of hepatorenal function and hematologic indices (Fig. 4A and Fig. S11-12). Thus, these results demonstrate that Cur-Cu@PEG exhibits acceptable biocompatibility and safety for further therapeutic applications in AKI.

The renal accumulation of NPs is beneficial for therapeutic efficiency during AKI progression [39]. RB is a typical fluorescent probe for tracking the distribution of nanomaterials in living organisms. Here, RB-labeled Cur-Cu@PEG was intravenously administered to RM-AKI and CP-AKI mice. The IVIS Lumina imaging system was utilized to investigate the targetability and biodistribution of RB-labeled Cur-Cu@PEG *in vivo*. Due to its ultra-small diameter, RB-labeled Cur-Cu@PEG exhibits renal accumulation in AKI mice at all time points appointed (Fig. 4B and D) [40]. Consistent with previous studies [41], deteriorative kidney function in AKI mice impedes the elimination of RB-labeled Cur-Cu@PEG, resulting in a longer duration of RB-labeled Cur-Cu@PEG in the renal tubules than healthy mice (Fig. 4C and E). Non-specific absorption of RB-labeled Cur-Cu@PEG in mouse livers was observed, possibly resulting from the moderate serum protein adsorption onto small spherical NPs *in vivo* [42]. Overall, Cur-Cu@PEG is kidney-targeted and exerts considerable kidney enrichment during AKI.

3.5. *Cur-Cu@PEG alleviates ROS-triggered AKI in vivo*

Given the ROS-scavenging properties of Cur-Cu@PEG, the ameliorative effects of Cur-Cu@PEG in oxidative stress-associated AKI models were further investigated. The negative and positive controls were AKI mice administered PBS and NAC, respectively [43]. Blood urea nitrogen (BUN) and serum creatinine (CRE) levels are reliable clinical kidney functional indicators [44,45]. Increased blood levels of BUN and CRE were observed in AKI mice. AKI mice administered Cur-Cu@PEG showed reduced serum BUN and CRE levels (Fig. 5B–C). Similarly, Cur-Cu@PEG suppressed the induced mRNA expression of the tubular injury marker NGAL in AKI mice (Fig. S13). H&E staining results indicated that massive amounts of denatured protein debris in tubule forms of AKI mice, namely renal tubular damage [46], were reduced in cohorts treated with Cur-Cu@PEG or NAC (Fig. 5D and Fig. S14). Moreover, Cur-Cu@PEG exhibited a significant inhibitory effect on immune cell infiltration in the kidneys of AKI mice (Fig. 5E). Next, the antioxidant capacity of Cur-Cu@PEG was assessed *in vivo*. Cur-Cu@PEG counteracted renal oxidative damage by hindering renal generation and accumulation of ROS (Fig. 6A). The levels of renal glutathione (GSH) were considered to decline in kidneys exposed to oxidative damage, accompanied by an excessive buildup of renal lipid peroxidation by-product malondialdehyde (MDA) [47,48]. Cur-Cu@PEG treatment elevated the amount of GSH with the corresponding decrease in MDA levels in AKI kidneys (Fig. 6B–C). The TUNEL assay further revealed that the number of injured renal tubular epithelial cells in Cur-Cu@PEG-treated mice was lower than that in model mice. Meanwhile, Cur-Cu@PEG exhibited superior therapeutic outcomes compared to NAC (Fig. 7A and Fig. S15). Altogether, Cur-Cu@PEG displayed robust ROS-scavenging properties in AKI kidneys and mitigated ROS-triggered AKI *in vivo*.

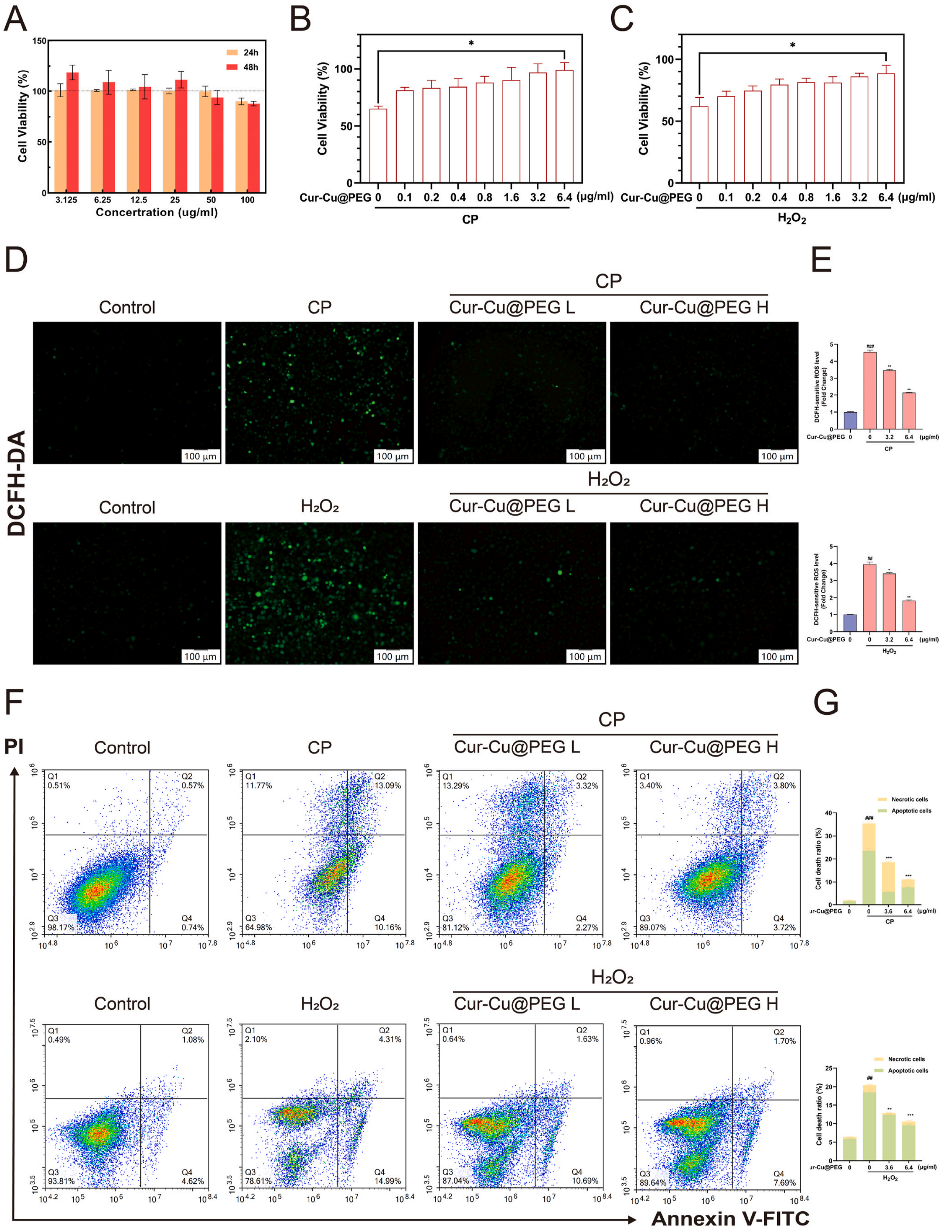

Fig. 3. Cur-Cu@PEG alleviates ROS-induced injury in HK-2 cells *in vitro*. **(A)** *In vitro* cell viability of HK-2 cells treated with Cur-Cu@PEG for 24 or 48 h. Mean ± S.D., $n = 4$. **(B–C)** Cell viability of HK-2 cells incubated with cisplatin (CP) (20 μM) (B) or H_2O_2 (400 μM) (C) with or without Cur-Cu@PEG pre-treatment. Mean ± S.D., $n = 3$. **(D–E)** Intracellular ROS fluorescence (D) and ROS levels (E) in HK-2 cells. Mean ± S.D., $n = 3$. **(F–G)** Flow cytometric analysis (F) and statistical analysis (G) of HK-2 cells. Mean ± S.D., $n = 3$. $^{\#\#}P < 0.01$, $^{\#\#\#}P < 0.001$ versus the control group; $^{*}P < 0.05$, $^{**}P < 0.01$, and $^{***}P < 0.001$ versus the CP/H_2O_2 group.

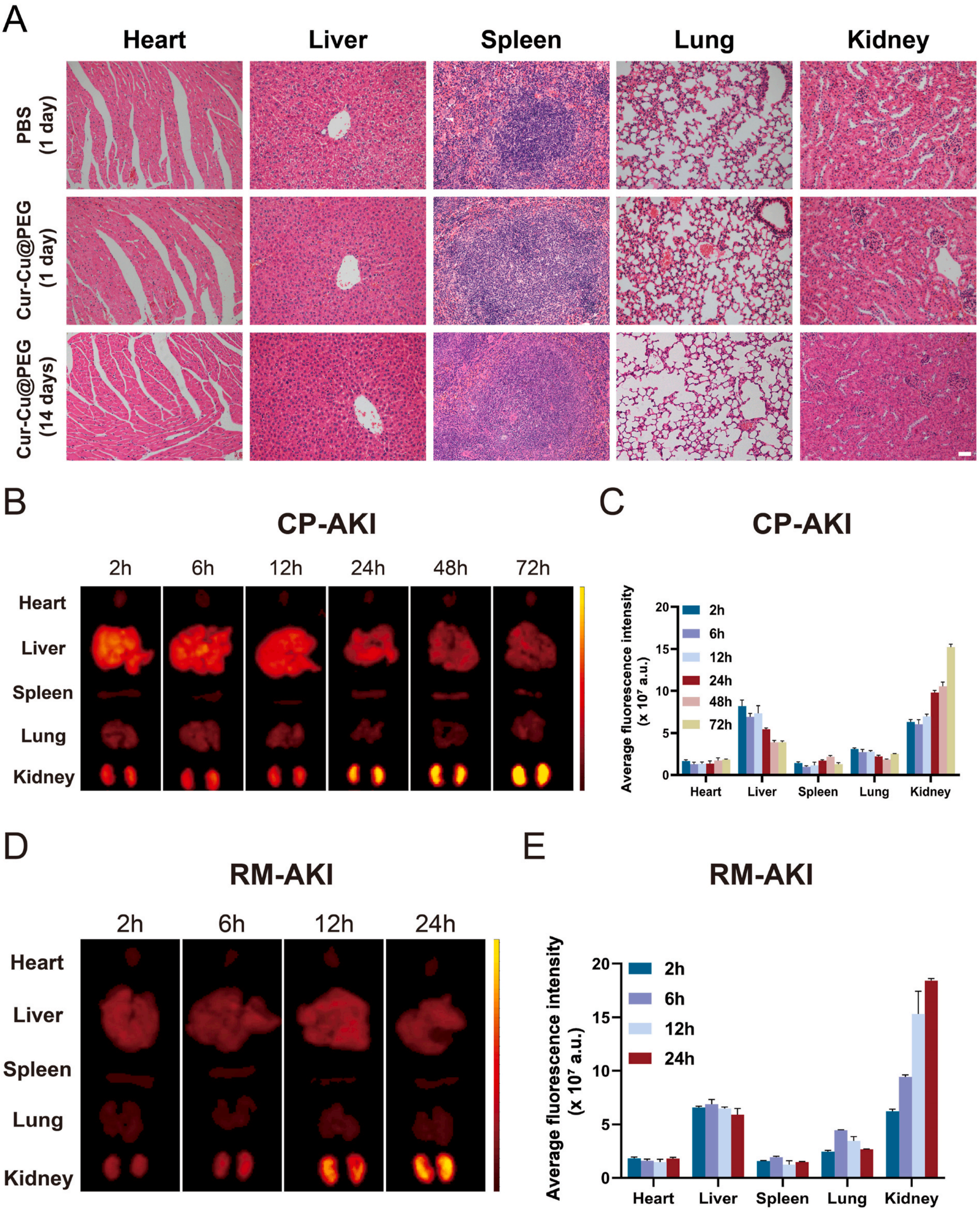

Fig. 4. Biocompatibility and biodistribution of PEG-modified Cur-Cu NPs *in vivo*. **(A)** Histological evaluation of primary organs, including heart, liver, spleen, lungs, and kidneys, in ICR mice intravenously administered with Cur-Cu@PEG (1 day or 14 days) or vehicle (1 day). Scale bar: 50 μm. **(B–E)** Representative IVIS images and average fluorescence intensities of primary organs obtained from cisplatin (CP)-induced AKI (CP-AKI) (B–C) and rhabdomyolysis (RM)-induced AKI (RM-AKI) (D–E) mice intravenously injected with Rhodamine B (RB)-labeled Cur-Cu@PEG. Mean ± S.D., $n = 3$.

3.6. Cur-Cu@PEG inhibits caspase-3-dependent apoptotic/pyroptotic cell death in kidneys of AKI mice

PCD induced by caspase-3 cleavage, including apoptosis and pyroptosis, is responsible for ROS-related AKI deterioration [49–51]. The immunohistochemistry and immunoblotting assays with an active caspase-3 antibody revealed that Cur-Cu@PEG administration limited ROS-triggered caspase-3 activation in AKI kidneys (Fig. 7B–C). As upstream activators of caspase-3, the proapoptotic Bax and antiapoptotic Bcl-2 govern the membrane-bound pore-forming process and interact through heterodimerization [52]. Immunoblotting assays further indicated that Cur-Cu@PEG treatment decreased the renal expression of Bax

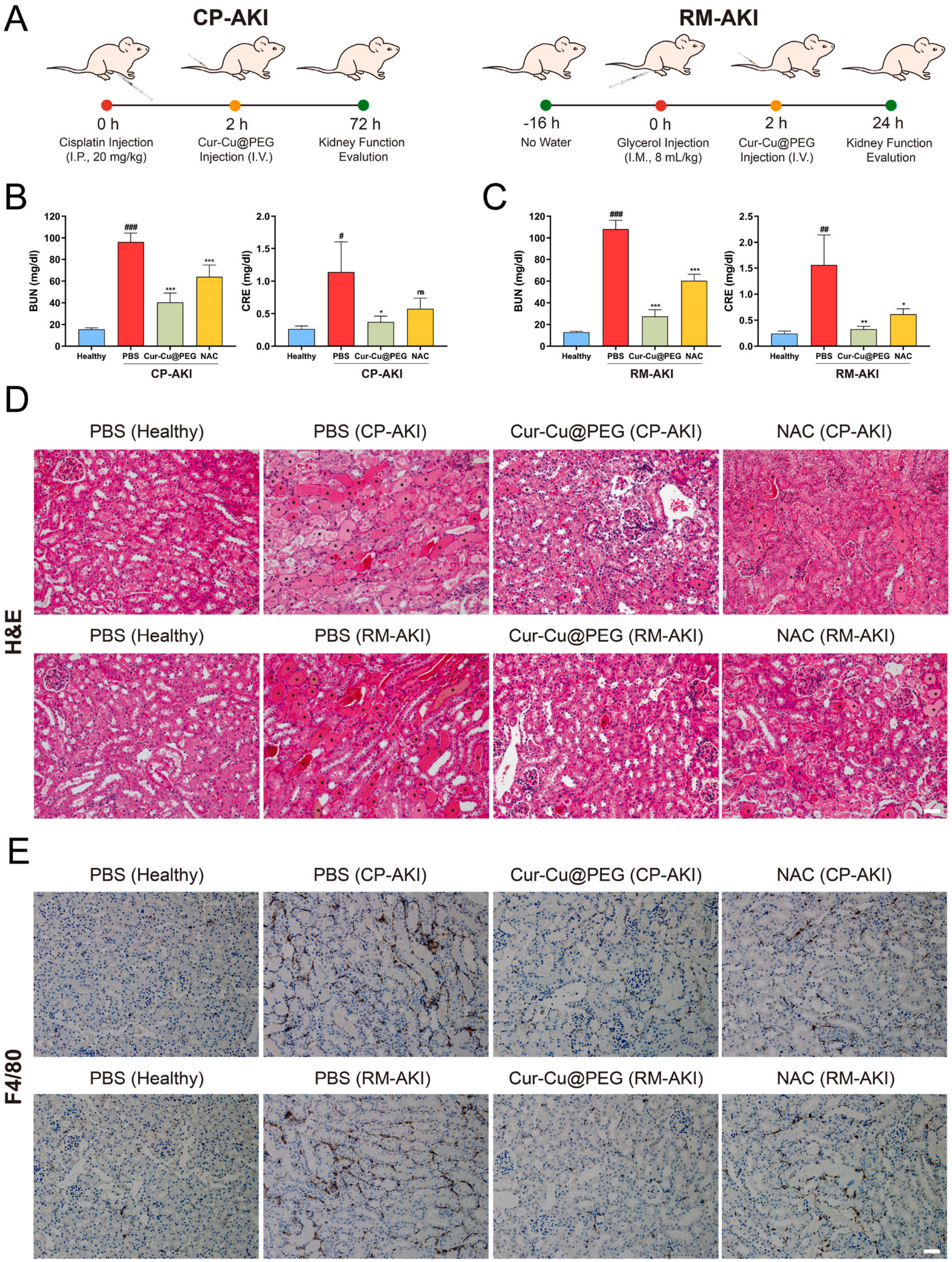

Fig. 5. Cur-Cu@PEG alleviates AKI *in vivo*. **(A)** Experimental design for AKI therapy. **(B–C)** Serum levels of blood urea nitrogen (BUN) and creatinine (CRE) in CP-AKI and RM-AKI mice. Mean ± S.D., $n = 6$. **(D)** H&E staining of representative kidney sections. Pentagrams indicate the formation of casts. **(E)** Representative images of F4/80-positive cells in kidney tissues. Scale bar: 50 μm. $^{\#}P < 0.05$, $^{\#\#}P < 0.01$, and $^{\#\#\#}P < 0.001$ versus the healthy group; $^{*}P < 0.05$, $^{**}P < 0.01$, and $^{***}P < 0.001$ versus the model group.

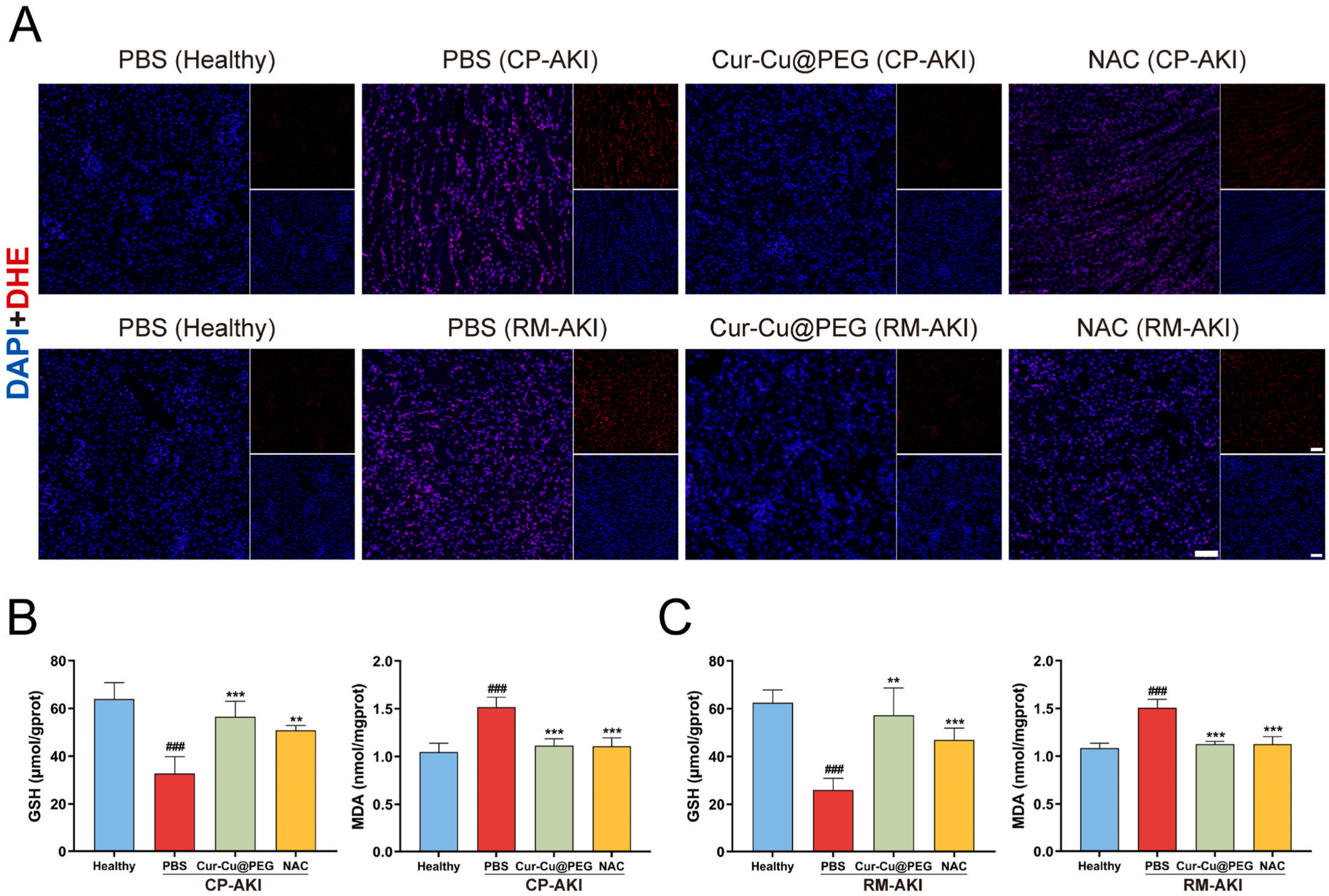

Fig. 6. Cur-Cu@PEG restrains renal oxidative stress in AKI mice. **(A)** Dihydroethidium (DHE) and DAPI staining of representative kidney sections. Scale bar: 50 μm. **(B–C)** Renal glutathione (GSH) levels and malondialdehyde (MDA) contents of groups in CP-AKI (B) and RM-AKI (C) mice. Mean ± S.D., $n = 6$. $^{###}P < 0.001$ versus the healthy group; $^{**}P < 0.01$, $^{***}P < 0.001$ versus the model group.

and Bax/Bcl-2 ratio in RM-AKI mice (Fig. 7C). The evidence suggests that Cur-Cu@PEG could restrain apoptosis in AKI kidneys. Moreover, pyroptosis is a new lytic form of PCD *via* membrane damage by pyroptotic effectors. Despite being known to trigger canonical apoptotic response, caspase-3 also participates in chemotherapy-induced pyroptotic cell death through GSDME cleavage [8]. Consistently, pyroptotic morphologic evidence suggested that noticeable swelling with distinct large bubbles originating from the plasma membrane in CP-treated HK-2 cells was mitigated by Cur-Cu@PEG (Fig. 8A). Scanning electron microscopy (SEM) further revealed that Cur-Cu@PEG treatment disturbed CP-induced massive pore formation of HK-2 cell membranes (Fig. 8B and Fig. S16). The release of LDH is considered a typical indication of pyroptotic cell cytotoxicity [8]. As shown in Fig. 8C, the LDH activity assay used for quantifying pyroptosis indicated that high lactate dehydrogenase levels in CP-treated cells were restored by Cur-Cu@PEG incubation. Together, these results suggest that Cur-Cu@PEG is capable of abolishing pyroptosis.

GSDME-dependent pyroptosis exacerbates CP-induced nephrotoxicity [7,53,54]. Cleaved caspase-3 contributes to full-length GSDME (GSDME-FL) cleaved to N-terminus GSDME (GSDME-N), which perforates membranes and thereby induces pyroptosis [8]. Consistently, the cleavage of GSDME and caspase-3 emerged in CP-incubated HK-2 cells *in vitro* (Fig. 8D–E). Notably, Cur-Cu@PEG treatment restrained the cleavage of caspase-3 and GSDME-FL, leading to a decrease in the production of GSDME-N (Fig. 8D–E). The translocase of outer mitochondrial membrane 20 (Tom20) is located in the outer mitochondrial membrane that senses and transmits ROS signaling, then facilitates Bax recruitment to mitochondria, ultimately leading to caspase-3 cleavage [9]. Cur-Cu@PEG demonstrates remarkable antioxidant properties, particularly excelling in scavenging •OH. Cur-Cu@PEG can efficiently neutralize ROS generated by CP, leading to a reduction in caspase-3 cleavage, further inhibiting the cleavage of GSDME, and ultimately suppressing pyroptosis. Immunoblotting analysis indicated that Cur-Cu@PEG treatment could downregulate the expression of Tom20 and Bax in CP-stimulated HK-2 cells (Fig. 8E). Similar effects on pyroptotic signaling were obtained in kidneys of AKI mice administered Cur-Cu@PEG (Fig. 8F).

In summary, the mechanistic evaluation indicates that Cur-Cu@PEG restrains ROS-evoked caspase-3-dependent apoptotic and pyroptotic cell death *in vitro* and AKI kidneys.

4. Conclusion

Collectively, a stable kidney-targeted ultrasmall nanozyme was fabricated as the antioxidant defense system for AKI therapy in the present study. Cur-Cu NPs possess robust antioxidant capacity. Cur-Cu@PEG effectively protects HK-2 cells against cellular oxidative damage *in vitro*. Also, Cur-Cu@PEG exerts exceptional biocompatibility, non-toxic, and kidney-targeted characteristics *in vivo*. Moreover, Cur-Cu@PEG shows apparent substantial therapeutic efficacy in AKI mice. Furthermore, Cur-Cu@PEG abolishes apoptotic/pyroptotic cell death of AKI kidneys by restraining the cleavage of caspase-3 *in vitro* and in mice.

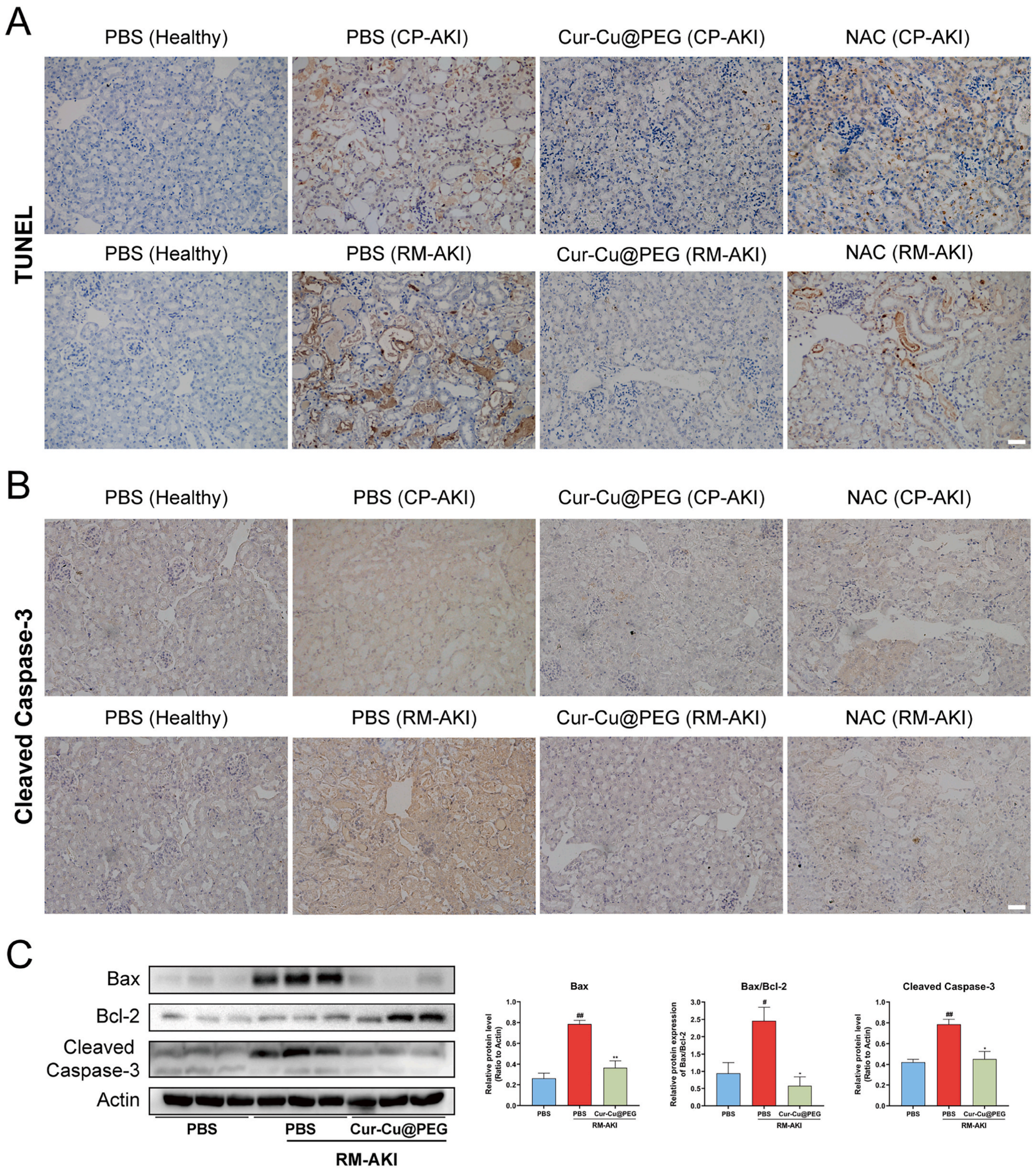

Fig. 7. Cur-Cu@PEG represses caspase-3-dependent programed cell death in kidneys of AKI mice. **(A–B)** Immunohistochemical staining of TUNEL (A) and cleaved caspase-3 (B) in kidneys of CP-AKI and RM-AKI mice. Scale bar: 50 μm. **(C)** Immunoblotting and densitometric analysis assessed protein expression levels of Bax, Bax/Bcl-2, and cleaved caspase-3 in kidney samples from RM-AKI mice. Mean ± S.D., *n* = 3. $^{\#}P < 0.05$, $^{\#\#}P < 0.01$ versus the PBS group; $^{*}P < 0.05$, $^{**}P < 0.01$ versus the PBS group from RM-AKI mice.

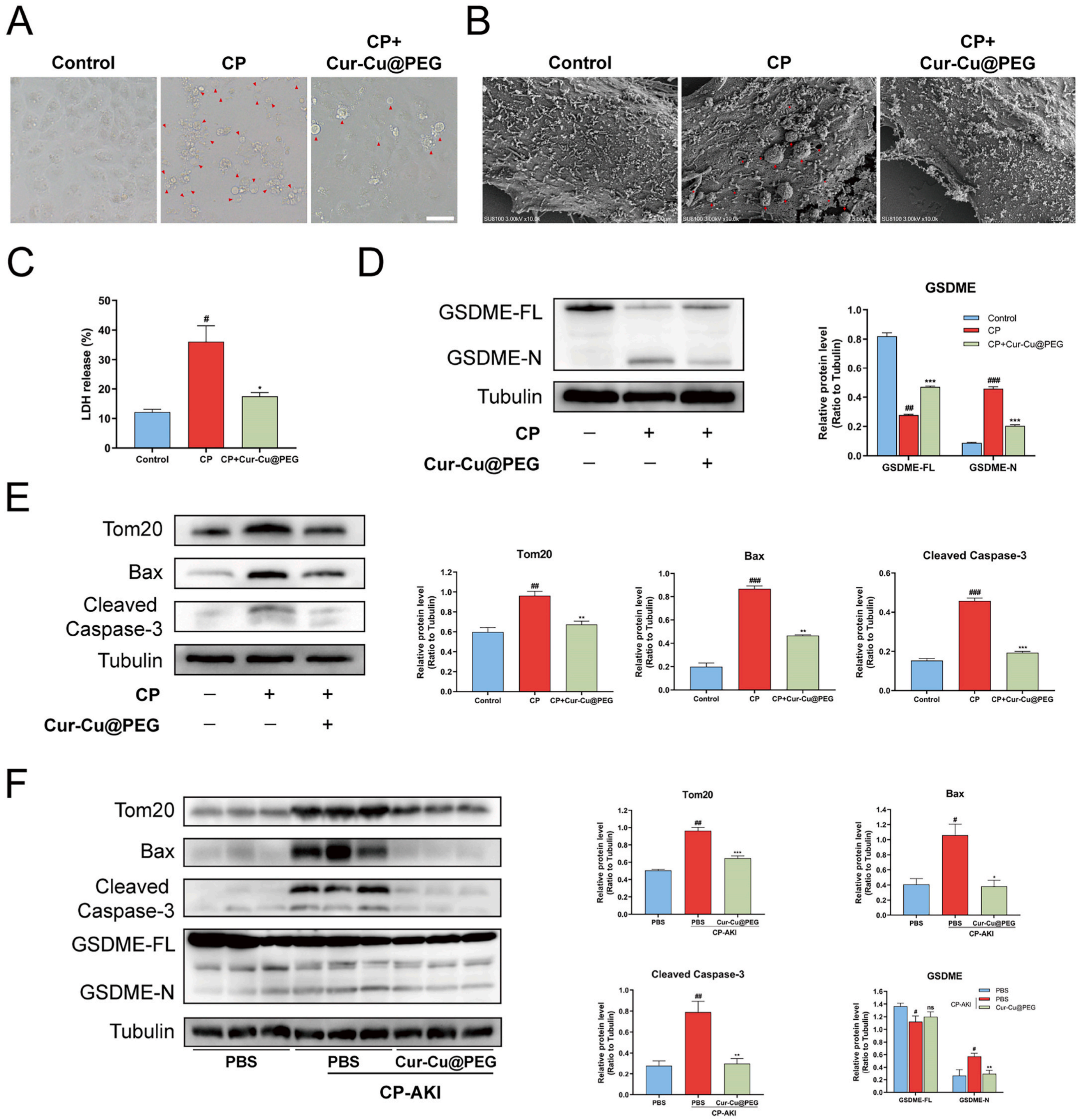

Fig. 8. Cur-Cu@PEG restrains caspase-dependent pyroptotic cell death *in vitro* and in kidneys of AKI mice. HK-2 cells were pretreated with Cur-Cu@PEG and consequently with CP (20 μM) for 24 h. Morphological changes of HK-2 cells were observed using light microscopy (A) or scanning electron microscopy (SEM) (B). **(A)** Red triangles indicate pyroptosis cells. Scale bar = 50 μm. **(B)** Red arrows represent bubbles originating from the plasma membrane, while the red pentagrams indicate pores emerging from the plasma membrane. Scale bar = 5 μm. **(C)** Lactate dehydrogenase (LDH) release assay. **(D–E)** Protein expression levels of GSDME cleavage (D), Tom20, Bax and cleaved caspase-3 (E) in HK-2 cells were evaluated by immunoblotting and densitometric analysis. **(F)** Immunoblotting and densitometric analysis of key effectors of caspase-3-dependent pyroptotic cell death in kidney samples of CP-AKI mice. Mean ± S.D., $n = 3$. $^{\#}P < 0.05$, $^{\#\#}P < 0.01$, and $^{\#\#\#}P < 0.001$ versus the control group; $^{*}P < 0.05$, $^{**}P < 0.01$, and $^{***}P < 0.001$ versus the CP group. $^{\#}P < 0.05$, $^{\#\#}P < 0.01$ versus the PBS group; $^{*}P < 0.05$, $^{**}P < 0.01$, and $^{***}P < 0.001$ versus the PBS group from CP-AKI mice. (For interpretation of the references to color in this figure legend, the reader is referred to the Web version of this article.)

Herein, the as-prepared Cur-Cu-based MPNs could be a promising therapeutic strategy for prevention of ROS-triggered AKI, offering valuable insights into developing nanomedicines for ameliorating ROS-related disorders.

CRediT authorship contribution statement

Xinyu Huang: Writing – original draft, Visualization, Investigation, Formal analysis, Data curation. **Fengxian Zhang:** Writing – original draft, Visualization, Formal analysis, Data curation. **Yuan Yang:** Writing – original draft, Visualization, Funding acquisition. **Jiawei Liu:** Validation, Data curation. **Xiangyun Tan:** Investigation, Data curation. **Peng Zhou:** Project administration. **Xiaolei Tang:** Funding acquisition. **Junjie Hu:** Visualization, Resources. **Liang Chen:** Visualization, Resources. **Ming Yuan:** Writing – original draft, Visualization, Funding acquisition. **Guohua Zheng:** Writing – review & editing, Project administration, Conceptualization. **Ziqiang Xu:** Writing – review & editing, Project administration, Funding acquisition, Conceptualization. **Zhenpeng Qiu:** Writing – review & editing, Supervision, Project administration, Funding acquisition, Conceptualization.

Declaration of competing interest

The authors declare that they have no known competing financial interests or personal relationships that could have appeared to influence the work reported in this paper.

Acknowledgements

This work was supported by the National Natural Science Foundation of China, China (Grant Nos. 82474130, 82074077, 22073025 and 32000278), the Open Project of Hubei Key Laboratory of Resources and Chemistry of Chinese Medicine, China (KLRCCM2404), the Open Project of Hubei Key Laboratory of Wudang Local Chinese Medicine Research (Hubei University of Medicine), China (Grant No. WDCM2023016), and the “Peak of Hope plan” talent project (the Second Affiliated Hospital of Wannan Medical College), China (Grant No. DFJH2022001).

Appendix A. Supplementary data

Supplementary data to this article can be found online at https://doi.org/10.1016/j.mtbio.2025.101794.

Data availability

Data will be made available on request.

References

[1] L.S. Chawla, P.W. Eggers, R.A. Star, P.L. Kimmel, Acute kidney injury and chronic kidney disease as interconnected syndromes, N. Engl. J. Med. 371 (1) (2014) 58–66, https://doi.org/10.1056/NEJMra1214243.

[2] Y. Wang, Y. Tao, Research progress on regulatory T cells in acute kidney injury, J Immunol Res 2015 (2015) 174164, https://doi.org/10.1155/2015/174164.

[3] Z. Hu, H. Zhang, B. Yi, S. Yang, J. Liu, J. Hu, J. Wang, K. Cao, W. Zhang, VDR activation attenuate cisplatin induced AKI by inhibiting ferroptosis, Cell Death Dis. 11 (1) (2020) 73, https://doi.org/10.1038/s41419-020-2256-z.

[4] C. Ronco, R. Bellomo, J.A. Kellum, Acute kidney injury, Lancet 394 (10212) (2019) 1949–1964, https://doi.org/10.1016/S0140-6736(19)32563-2.

[5] A. Zuk, J.V. Bonventre, Acute kidney injury, Annu. Rev. Med. 67 (2016) 293–307, https://doi.org/10.1146/annurev-med-050214-013407.

[6] J.Y.C. Soo, J. Jansen, R. Masereeuw, M.H. Little, Advances in predictive in vitro models of drug-induced nephrotoxicity, Nat. Rev. Nephrol. 14 (6) (2018) 378–393, https://doi.org/10.1038/s41581-018-0003-9.

[7] X. Shen, H. Wang, C. Weng, H. Jiang, J. Chen, Caspase 3/GSDME-dependent pyroptosis contributes to chemotherapy drug-induced nephrotoxicity, Cell Death Dis. 12 (2) (2021) 186, https://doi.org/10.1038/s41419-021-03458-5.

[8] Y. Wang, W. Gao, X. Shi, J. Ding, W. Liu, H. He, K. Wang, F. Shao, Chemotherapy drugs induce pyroptosis through caspase-3 cleavage of a gasdermin, Nature 547 (7661) (2017) 99–103, https://doi.org/10.1038/nature22393.

[9] B. Zhou, J.-Y. Zhang, X.-S. Liu, H.-Z. Chen, Y.-L. Ai, K. Cheng, R.-Y. Sun, D. Zhou, J. Han, Q. Wu, Tom20 senses iron-activated ROS signaling to promote melanoma cell pyroptosis, Cell Res. 28 (12) (2018) 1171–1185, https://doi.org/10.1038/s41422-018-0090-y.

[10] J. Belliere, A. Casemayou, L. Ducasse, A. Zakaroff-Girard, F. Martins, J.S. Iacovoni, C. Guilbeau-Frugier, B. Buffin-Meyer, B. Pipy, D. Chauveau, J.P. Schanstra, J.-L. Bascands, Specific macrophage subtypes influence the progression of rhabdomyolysis-induced kidney injury, J. Am. Soc. Nephrol. 26 (6) (2015) 1363–1377, https://doi.org/10.1681/ASN.2014040320.

[11] X. Bosch, E. Poch, J.M. Grau, Rhabdomyolysis and acute kidney injury, N. Engl. J. Med. 361 (1) (2009) 62–72, https://doi.org/10.1056/NEJMra0801327.

[12] S. Fishbane, N-acetylcysteine in the prevention of contrast-induced nephropathy, Clin. J. Am. Soc. Nephrol. 3 (1) (2008) 281–287, https://doi.org/10.2215/CJN.02590607.

[13] X. Ma, J. Hao, J. Wu, Y. Li, X. Cai, Y. Zheng, Prussian blue nanozyme as a pyroptosis inhibitor alleviates neurodegeneration, Adv. Mater. 34 (15) (2022) e2106723, https://doi.org/10.1002/adma.202106723.

[14] Y. Liu, Y. Cheng, H. Zhang, M. Zhou, Y. Yu, S. Lin, B. Jiang, X. Zhao, L. Miao, C.-W. Wei, Q. Liu, Y.-W. Lin, Y. Du, C.J. Butch, H. Wei, Integrated cascade nanozyme catalyzes *in vivo* ROS scavenging for anti-inflammatory therapy, Sci. Adv. 6 (29) (2020) eabb2695, https://doi.org/10.1126/sciadv.abb2695.

[15] Z. Wei, G. Peng, Y. Zhao, S. Chen, R. Wang, H. Mao, Y. Xie, C. Zhao, Engineering antioxidative cascade metal-phenolic nanozymes for alleviating oxidative stress during extracorporeal blood purification, ACS Nano 16 (11) (2022) 18329–18343, https://doi.org/10.1021/acsnano.2c06186.

[16] Z. Xu, G. Liu, J. Huang, J. Wu, Novel glucose-responsive antioxidant hybrid hydrogel for enhanced diabetic wound repair, ACS Appl. Mater. Interfaces 14 (6) (2022) 7680–7689, https://doi.org/10.1021/acsami.1c23461.

[17] Z. Wei, L. Wang, C. Tang, S. Chen, Z. Wang, Y. Wang, J. Bao, Y. Xie, W. Zhao, B. Su, C. Zhao, Metal-phenolic networks nanoplatform to mimic antioxidant defense system for broad-spectrum radical eliminating and endotoxemia treatment, Adv. Funct. Mater. 30 (49) (2020) 2002234, https://doi.org/10.1002/adfm.202002234.

[18] Y. Xie, S. Chen, X. Peng, X. Wang, Z. Wei, J.J. Richardson, K. Liang, H. Ejima, J. Guo, C. Zhao, Alloyed nanostructures integrated metal-phenolic nanoplatform for synergistic wound disinfection and revascularization, Bioact. Mater. 16 (2022) 95–106, https://doi.org/10.1016/j.bioactmat.2022.03.004.

[19] D. Wu, J. Zhou, M.N. Creyer, W. Yim, Z. Chen, P.B. Messersmith, J.V. Jokerst, Phenolic-enabled nanotechnology: versatile particle engineering for biomedicine, Chem. Soc. Rev. 50 (7) (2021) 4432–4483, https://doi.org/10.1039/d0cs00908c.

[20] K. Li, G. Xiao, J.J. Richardson, B.L. Tardy, H. Ejima, W. Huang, J. Guo, X. Liao, B. Shi, Targeted therapy against metastatic melanoma based on self-assembled metal-phenolic nanocomplexes comprised of green tea catechin, Adv. Sci. (Weinh.) 6 (5) (2019) 1801688, https://doi.org/10.1002/advs.201801688.

[21] H. Geng, Q.-Z. Zhong, J. Li, Z. Lin, J. Cui, F. Caruso, J. Hao, Metal ion-directed functional metal-phenolic materials, Chem. Rev. 122 (13) (2022) 11432–11473, https://doi.org/10.1021/acs.chemrev.1c01042.

[22] H. Yuan, F. Wang, Z. Wang, D. Gu, W. Huang, C. Fu, X. Wang, J. Ma, Z. Li, L. Dai, X. Zhang, W. Xiao, J. Wang, Natural metal polyphenol nanozyme: free radical scavenging and antioxidation for the treatment of acute kidney injury, ACS Mater. Lett. 5 (10) (2023) 2807–2819, https://doi.org/10.1021/acsmaterialslett.3c00906.

[23] Y. Li, Y. Miao, L. Yang, Y. Zhao, K. Wu, Z. Lu, Z. Hu, J. Guo, Recent advances in the development and antimicrobial applications of metal–phenolic networks, Adv. Sci. 9 (27) (2022) 2202684, https://doi.org/10.1002/advs.202202684.

[24] T. Liu, B. Xiao, F. Xiang, J. Tan, Z. Chen, X. Zhang, C. Wu, Z. Mao, G. Luo, X. Chen, J. Deng, Ultrasmall copper-based nanoparticles for reactive oxygen species scavenging and alleviation of inflammation related diseases, Nat. Commun. 11 (1) (2020) 2788, https://doi.org/10.1038/s41467-020-16544-7.

[25] E. Phillips, O. Penate-Medina, P.B. Zanzonico, R.D. Carvajal, P. Mohan, Y. Ye, J. Humm, M. Gönen, H. Kalaigian, H. Schöder, H.W. Strauss, S.M. Larson, U. Wiesner, M.S. Bradbury, Clinical translation of an ultrasmall inorganic optical-PET imaging nanoparticle probe, Sci. Transl. Med. 6 (260) (2014), https://doi.org/10.1126/scitranslmed.3009524, 260ra149.

[26] F. Gao, J. Huang, Y. Ruan, H. Li, P. Gong, F. Wang, Q. Tang, Y. Jiang, Unraveling the structure transition and peroxidase mimic activity of copper sites over atomically dispersed copper-doped carbonized polymer dots, Angew Chem. Int. Ed. Engl. 62 (7) (2023) e202214042, https://doi.org/10.1002/anie.202214042.

[27] Z. Lyu, S. Zhu, M. Xie, Y. Zhang, Z. Chen, R. Chen, M. Tian, M. Chi, M. Shao, Y. Xia, Controlling the surface oxidation of Cu nanowires improves their catalytic selectivity and stability toward C_{2+} products in CO_2 reduction, Angew Chem. Int. Ed. Engl. 60 (4) (2021) 1909–1915, https://doi.org/10.1002/anie.202011956.

[28] J. Yang, R. Zhang, H. Zhao, H. Qi, J. Li, J.-F. Li, X. Zhou, A. Wang, K. Fan, X. Yan, T. Zhang, Bioinspired copper single-atom nanozyme as a superoxide dismutase-like antioxidant for sepsis treatment, Explorations 2 (4) (2022) 20210267, https://doi.org/10.1002/EXP.20210267.

[29] D.B. Zorov, M. Juhaszova, S.J. Sollott, Mitochondrial reactive oxygen species (ROS) and ROS-induced ROS release, Physiol. Rev. 94 (3) (2014) 909–950, https://doi.org/10.1152/physrev.00026.2013.

[30] F. Gao, J. Liu, P. Gong, Y. Yang, Y. Jiang, Carbon dots as potential antioxidants for the scavenging of multi-reactive oxygen and nitrogen species, Chem. Eng. J. 462 (2023) 142338, https://doi.org/10.1016/j.cej.2023.142338.

[31] J. Liu, X. Huang, F. Zhang, X. Luo, W. Yu, C. Li, Z. Qiu, Y. Liu, Z. Xu, Metal-free multifunctional nanozymes mimicking endogenous antioxidant system for acute kidney injury alleviation, Chem. Eng. J. 477 (2023) 147048, https://doi.org/10.1016/j.cej.2023.147048.

[32] K. Wang, Y. Zhang, W. Mao, W. Feng, S. Lu, J. Wan, X. Song, Y. Chen, B. Peng, Engineering ultrasmall ferroptosis-targeting and reactive oxygen/nitrogen species-

scavenging nanozyme for alleviating acute kidney injury, Adv. Funct. Mater. 32 (10) (2022) 2109221, https://doi.org/10.1002/adfm.202109221.

[33] F. Wu, Y. Du, J. Yang, B. Shao, Z. Mi, Y. Yao, Y. Cui, F. He, Y. Zhang, P. Yang, Peroxidase-like active nanomedicine with dual glutathione depletion property to restore oxaliplatin chemosensitivity and promote programmed cell death, ACS Nano 16 (3) (2022) 3647–3663, https://doi.org/10.1021/acsnano.1c06777.

[34] C. Zhou, L. Zhang, Z. Xu, T. Sun, M. Gong, Y. Liu, D. Zhang, Self-propelled ultrasmall AuNPs-tannic acid hybrid nanozyme with ROS-scavenging and anti-inflammatory activity for drug-induced liver injury alleviation, Small 19 (19) (2023) e2206408, https://doi.org/10.1002/smll.202206408.

[35] J.R. Arthur, The glutathione peroxidases, Cell. Mol. Life. Sci. 57 (13) (2001) 1825–1835, https://doi.org/10.1007/PL00000664.

[36] J. Liu, L. Shi, Y. Wang, M. Li, C. Zhou, L. Zhang, C. Yao, Y. Yuan, D. Fu, Y. Deng, M. Liu, G. Wang, L. Wang, Z. Wang, Ruthenium-based metal-organic framework with reactive oxygen and nitrogen species scavenging activities for alleviating inflammation diseases, Nano Today 47 (2022) 101627, https://doi.org/10.1016/j.nantod.2022.101627.

[37] D.-H. Kim, H.-I. Choi, J.S. Park, C.S. Kim, E.H. Bae, S.K. Ma, S.W. Kim, Farnesoid X receptor protects against cisplatin-induced acute kidney injury by regulating the transcription of ferroptosis-related genes, Redox Biol. 54 (2022) 102382, https://doi.org/10.1016/j.redox.2022.102382.

[38] S. Jin, Q.Y. Zhang, X.M. Kang, J.X. Wang, W.H. Zhao, Daidzein induces MCF-7 breast cancer cell apoptosis via the mitochondrial pathway, Ann. Oncol. 21 (2) (2010) 263–268, https://doi.org/10.1093/annonc/mdp499.

[39] Y. Huang, J. Wang, K. Jiang, E.J. Chung, Improving kidney targeting: the influence of nanoparticle physicochemical properties on kidney interactions, J. Contr. Release 334 (2021) 127–137, https://doi.org/10.1016/j.jconrel.2021.04.016.

[40] T.A. Sutton, C.J. Fisher, B.A. Molitoris, Microvascular endothelial injury and dysfunction during ischemic acute renal failure, Kidney Int. 62 (5) (2002) 1539–1549, https://doi.org/10.1046/j.1523-1755.2002.00631.x.

[41] J. Gao, Y. Liu, B. Jiang, W. Cao, Y. Kan, W. Chen, M. Ding, G. Zhang, B. Zhang, K. Xi, X. Jia, X. Zhao, H. Guo, Phenylenediamine-based carbon nanodots alleviate acute kidney injury via preferential renal accumulation and antioxidant capacity, ACS Appl. Mater. Interfaces 12 (28) (2020) 31745–31756, https://doi.org/10.1021/acsami.0c05041.

[42] K.-R. Kim, J. Kim, J.H. Back, J.E. Lee, D.-R. Ahn, Cholesterol-Mediated seeding of protein corona on DNA nanostructures for targeted delivery of oligonucleotide therapeutics to treat liver fibrosis, ACS Nano 16 (5) (2022) 7331–7343, https://doi.org/10.1021/acsnano.1c08508.

[43] D.-Y. Zhang, T. Tu, M.R. Younis, K.S. Zhu, H. Liu, S. Lei, J. Qu, J. Lin, P. Huang, Clinically translatable gold nanozymes with broad spectrum antioxidant and anti-inflammatory activity for alleviating acute kidney injury, Theranostics 11 (20) (2021) 9904–9917, https://doi.org/10.7150/thno.66518.

[44] D. Jiang, Z. Ge, H.-J. Im, C.G. England, D. Ni, J. Hou, L. Zhang, C.J. Kutyreff, Y. Yan, Y. Liu, S.Y. Cho, J.W. Engle, J. Shi, P. Huang, C. Fan, H. Yan, W. Cai, DNA origami nanostructures can exhibit preferential renal uptake and alleviate acute kidney injury, Nat. Biomed. Eng. 2 (11) (2018) 865–877, https://doi.org/10.1038/s41551-018-0317-8.

[45] J. Huang, J. Li, Y. Lyu, Q. Miao, K. Pu, Molecular optical imaging probes for early diagnosis of drug-induced acute kidney injury, Nat. Mater. 18 (10) (2019) 1133–1143, https://doi.org/10.1038/s41563-019-0378-4.

[46] Q. Weng, H. Sun, C. Fang, F. Xia, H. Liao, J. Lee, J. Wang, A. Xie, J. Ren, X. Guo, F. Li, B. Yang, D. Ling, Catalytic activity tunable ceria nanoparticles prevent chemotherapy-induced acute kidney injury without interference with chemotherapeutics, Nat. Commun. 12 (1) (2021) 1436, https://doi.org/10.1038/s41467-021-21714-2.

[47] S.-Y. Peng, X.-H. Liu, Q.-W. Chen, Y.-J. Yu, M.-D. Liu, X.-Z. Zhang, Harnessing in situ glutathione for effective ROS generation and tumor suppression via nanohybrid-mediated catabolism dynamic therapy, Biomaterials 281 (2022) 121358, https://doi.org/10.1016/j.biomaterials.2021.121358.

[48] S.J. Dixon, K.M. Lemberg, M.R. Lamprecht, R. Skouta, E.M. Zaitsev, C.E. Gleason, D.N. Patel, A.J. Bauer, A.M. Cantley, W.S. Yang, B. Morrison, B.R. Stockwell, Ferroptosis: an iron-dependent form of nonapoptotic cell death, Cell 149 (5) (2012) 1060–1072, https://doi.org/10.1016/j.cell.2012.03.042.

[49] M. D'Amelio, V. Cavallucci, F. Cecconi, Neuronal caspase-3 signaling: not only cell death, Cell Death Differ. 17 (7) (2010) 1104–1114, https://doi.org/10.1038/cdd.2009.180.

[50] M. Gao, Q. Sun, H. Zhang, M. Liu, R. Peng, W. Qin, Q. Wang, T. Yang, M. Zhou, X. He, G. Sun, Bioinspired nano-photosensitizer-activated caspase-3/GSDME pathway induces pyroptosis in lung cancer cells, Adv. Healthcare Mater. (2024) e2401616, https://doi.org/10.1002/adhm.202401616.

[51] H. Yu, F. Jin, D. Liu, G. Shu, X. Wang, J. Qi, M. Sun, P. Yang, S. Jiang, X. Ying, Y. Du, ROS-responsive nano-drug delivery system combining mitochondria-targeting ceria nanoparticles with atorvastatin for acute kidney injury, Theranostics 10 (5) (2020) 2342–2357, https://doi.org/10.7150/thno.40395.

[52] J. Misao, Y. Hayakawa, M. Ohno, S. Kato, T. Fujiwara, H. Fujiwara, Expression of bcl-2 protein, an inhibitor of apoptosis, and Bax, an accelerator of apoptosis, in ventricular myocytes of human hearts with myocardial infarction, Circulation 94 (7) (1996) 1506–1512, https://doi.org/10.1161/01.cir.94.7.1506.

[53] Y. Li, Y. Yuan, Z.-X. Huang, H. Chen, R. Lan, Z. Wang, K. Lai, H. Chen, Z. Chen, Z. Zou, H.-B. Ma, H.-Y. Lan, T.W. Mak, Y. Xu, GSDME-mediated pyroptosis promotes inflammation and fibrosis in obstructive nephropathy, Cell Death Differ. 28 (8) (2021) 2333–2350, https://doi.org/10.1038/s41418-021-00755-6.

[54] W. Xia, Y. Li, M. Wu, Q. Jin, Q. Wang, S. Li, S. Huang, A. Zhang, Y. Zhang, Z. Jia, Gasdermin E deficiency attenuates acute kidney injury by inhibiting pyroptosis and inflammation, Cell Death Dis. 12 (2) (2021) 139, https://doi.org/10.1038/s41419-021-03431-2.